Nanoparticle Imaging Probes for Molecular Imaging with Computed Tomography and Application to Cancer Imaging

Ryan K. Roeder,*[a,b] Tyler E. Curtis,[a] Prakash D. Nallathamby,[a,b] Lisa E. Irimata,[a,b]
Tracie L. McGinnity,[a,b] Lisa E. Cole,[a,b] Tracy Vargo-Gogola,[b,c] and Karen D. Cowden Dahl[b,c]

[a]Department of Aerospace and Mechanical Engineering, Bioengineering Graduate Program, University of Notre Dame, Notre Dame, IN 46556, USA; [b]Harper Cancer Research Institute, University of Notre Dame, Notre Dame, IN 46556, USA; [c]Department of Biochemistry and Molecular Biology, Indiana University Simon Cancer Center, Indiana University School of Medicine – South Bend, South Bend, IN 46617, USA

ABSTRACT

Precision imaging is needed to realize precision medicine in cancer detection and treatment. Molecular imaging offers the ability to target and identify tumors, associated abnormalities, and specific cell populations with overexpressed receptors. Nuclear imaging and radionuclide probes provide high sensitivity but subject the patient to a high radiation dose and provide limited spatiotemporal information, requiring combined computed tomography (CT) for anatomic imaging. Therefore, nanoparticle contrast agents have been designed to enable molecular imaging and improve detection in CT alone. Core-shell nanoparticles provide a powerful platform for designing tailored imaging probes. The composition of the core is chosen for enabling strong X-ray contrast, multi-agent imaging with photon-counting spectral CT, and multimodal imaging. A silica shell is used for protective, biocompatible encapsulation of the core composition, volume-loading fluorophores or radionuclides for multimodal imaging, and facile surface functionalization with antibodies or small molecules for targeted delivery. Multi-agent (*k*-edge) imaging and quantitative molecular imaging with spectral CT was demonstrated using current clinical agents (iodine and $BaSO_4$) and a proposed spectral library of contrast agents (Gd_2O_3, HfO_2, and Au). Bisphosphonate-functionalized Au nanoparticles were demonstrated to enhance sensitivity and specificity for the detection of breast microcalcifications by conventional radiography and CT in both normal and dense mammary tissue using murine models. Moreover, photon-counting spectral CT enabled quantitative material decomposition of the Au and calcium signals. Immunoconjugated Au@SiO_2 nanoparticles enabled highly-specific targeting of CD133+ ovarian cancer stem cells for contrast-enhanced detection in model tumors.

Keywords: Cancer, Contrast Agent, Molecular Imaging, Nanoparticles, Photon-Counting Spectral CT, Precision Medicine, X-ray Computed Tomography

1. PURPOSE

Precision imaging is critical to the realization of precision medicine in oncology. Molecular imaging approaches have the potential to overcome obstacles to precision oncology by enabling early detection and discovery of biomarkers, noninvasive monitoring of recurrence and therapeutic response, and characterization of heterogeneity in tumor microenvironment and cell populations [1-3]. Molecular imaging with computed tomography (CT) could offer a single, low cost and widely available modality for combined molecular and anatomic imaging at high spatiotemporal resolution [4]. Nanoparticles (NPs) comprising high-*Z* metals, such as Au, have gained recent interest as X-ray contrast agents due to enabling the delivery of a greater mass payload compared with molecular contrast agents (e.g., iodinated molecules and Gd-chelates) used clinically [5,6]. NP imaging probes can thus be designed for strong X-ray contrast, biostability, multimodal/multi-agent imaging, and targeted delivery [5-9]. Concomitant developments in photon-counting spectral CT are also transforming the capabilities of CT by enabling quantitative multi-material decomposition [10]. Therefore, the objective of this paper is to present an emerging strategy where engineered NP imaging probes and photon-counting detectors act synergistically to enable quantitative molecular imaging with CT for precision imaging in cancer detection and treatment. Examples of emerging capabilities are presented including quantitative molecular imaging of tumors, associated abnormalities (e.g., microcalcifications), multiple probe/tissue compositions, and cell populations overexpressing biomarkers using both conventional CT and photon-counting spectral CT.

---

* rroeder@nd.edu; phone 574-631-7003; https://engineering.nd.edu/profiles/rroeder

Medical Imaging 2017: Physics of Medical Imaging, edited by Thomas G. Flohr,
Joseph Y. Lo, Taly Gilat Schmidt, Proc. of SPIE Vol. 10132, 101320X · © 2017 SPIE
CCC code: 1605-7422/17/$18 · doi: 10.1117/12.2255688

2. MULTI-AGENT AND MULTI-MATERIAL IMAGING

2.1. Significance

X-ray imaging has been the primary means of non-invasive imaging in biomedicine for the last century. Radiography was revolutionized in the 1970s by the advent of 3D CT which has become the "first-line" modality for cancer imaging due to high spatiotemporal resolution, low cost, and wide availability [11-13]. The primary limitation of CT has been a relatively low sensitivity and lack of molecular imaging capabilities, which has fueled the use of more costly adjunct imaging methods such as magnetic resonance imaging (MRI), positron emission tomography (PET), and single photon emission computed tomography (SPECT). PET and SPECT provide high sensitivity but require radiopharmaceuticals and provide limited spatiotemporal information, thus requiring combined CT for anatomic imaging and subjecting the patient to a high radiation dose [14,15]. Therefore, the ability to perform quantitative multi-agent and multi-material imaging with photon-counting spectral CT has the potential to usher in a new revolution in biomedical imaging, enabling precision imaging of multiple targets/tissues in cancer detection and treatment.

2.2. Materials and Methods

Imaging phantoms were prepared comprising Au NPs [6,16], HfO_2 NPs [9], and iodine (iohexol). Note that Au NPs have become the most prominent NP X-ray contrast agent used in preclinical research, HfO_2 NPs are a novel contrast agent leveraging the favorable location of the Hf *k*-edge near the mean photon energy of clinical CT systems, and iodine is the most prominent X-ray contrast agent used in clinical diagnostic imaging [6,9]. Contrast agent solutions were prepared at 10, 20, and 50 mM concentrations and dispersed in 1% agarose to maintain homogeneity and stability over a period of months. Aliquots of each agent and concentration were pipetted into separate Eppendorf tubes and solidified rapidly on ice. An excised rabbit femur was also embedded in 1% agarose and imaged as an additional control sample for comparison. Note that the background attenuation due to agarose in the phantoms was verified to be negligible. The accuracy of concentrations was also verified for Au NPs using inductively coupled plasma-optical emission spectroscopy after digesting samples in 3% aqua regia.

Phantoms were imaged using commercially-available photon-counting spectral micro-CT (MARS Bioimaging Ltd., Christchurch, NZ) with a 120 kVp source and ~100 μm voxel size. Conventional CT images were acquired using a single energy bin (33.1-65.0 keV) selected for the range with the highest photon count rate in typical clinical imaging systems. Measured linear attenuation coefficients were converted to Hounsfield units (HU) using an internal sample calibration with the mean linear attenuation coefficients measured for air (-1000 HU) and water (0 HU). Spectral CT used a photon-counting detector comprising a CdZnTe semiconductor bonded to a Medipix3RX ASIC (CERN) which enabled simultaneous image acquisitions within multiple energy bins [17], which were set to 7.0-14.8, 14.8-33.1, 33.1-65.0, 65.0-80.1, and 80.1-120 keV, in order to leverage the *k*-edge of iodine (33.2 keV), hafnium (65.4 keV), and gold (80.7 keV). Quantitative material decomposition was performed using a quadratic programming algorithm (Matlab v9.0) with a maximum *a posteriori* estimator [18]. The material decomposition algorithm was calibrated to known concentrations including: 50 mM contrast agent concentrations, a bone mimicking composition containing 40 vol% hydroxyapatite [19], acrylic plastic, 1% agarose, and water. The fractional abundance of Au, Hf, and I were then assigned to RGB channels, respectively, and scaled to mM concentrations.

A subcutaneous injection of 0.25 mL of 20 mM Gd_2O_3 NPs in 1% agarose was administered to a mouse post-mortem to demonstrate quantitative molecular imaging with photon-counting spectral CT compared to conventional CT image slices and reconstructions. Image acquisition and materials decomposition used the same methods described above except that energy bins were tailored to the *k*-edge of Gd (50.2 keV).

3.3. Results and Discussion

In conventional CT images, multiple contrast agents (Au NPs, HfO_2 NPs, and iodine) were indistinguishable from each other and exhibited weak signal relative to adjacent bone tissue (Fig. 1), such that a contrast agent (Gd_2O_3) administered to an animal was not readily distinguished from bone (Fig. 2). In contrast, photon-counting spectral CT enabled simultaneous color delineation and quantitative molecular imaging of each contrast agent (Fig. 1). Accurate quantitative multi-material decomposition was enabled by energy-dependent differences in the X-ray attenuation of each material. Each contrast agent was also able to be clearly distinguished from bone and water (or soft tissue) in spectral CT (Figs. 1 and 2), although a small amount of erroneous Au signal was observed immediately adjacent to the bone phantom, likely due to beam hardening (Fig. 1). Note that concentrations of 10-50 mM are representative of the mass concentration of contrast agent that can be delivered to a targeted site of interest in preclinical animal models [6]. Thus, photon-counting detectors and NP contrast agents may act synergistically to transform CT into a quantitative molecular imaging modality capable of multi-agent/material imaging in preclinical animal models.

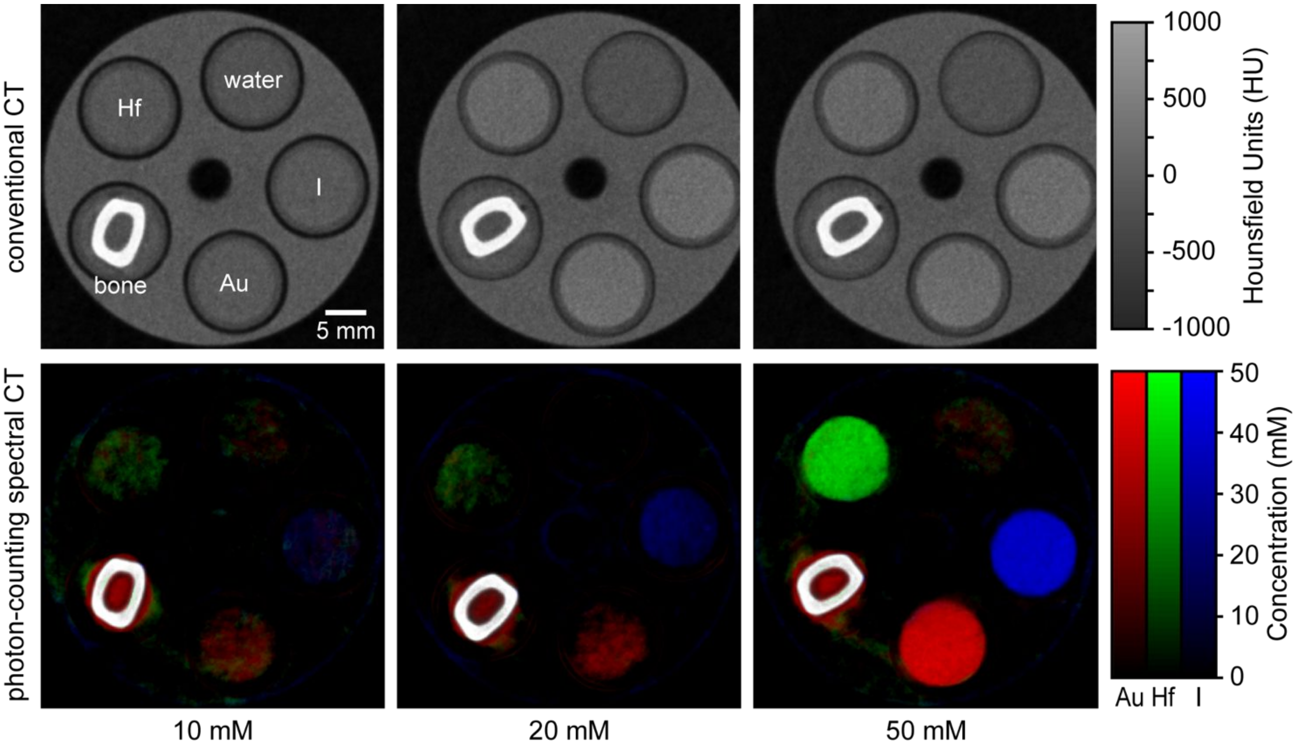

Figure 1. Conventional and photon-counting spectral CT (MARS Bioimaging) images of phantoms containing (clockwise from top) water, Au NPs (red), iodine (blue), a rabbit femur (white), and HfO_2 NPs (green), at 10, 20, and 50 mM contrast agent concentrations. Photon-counting spectral CT enabled clear, color delineation and quantitative molecular imaging of multiple contrast agent compositions, at concentrations suitable for *in vivo* delivery, and multiple tissues (bone and water), which were not able to be distinguished in conventional CT images.

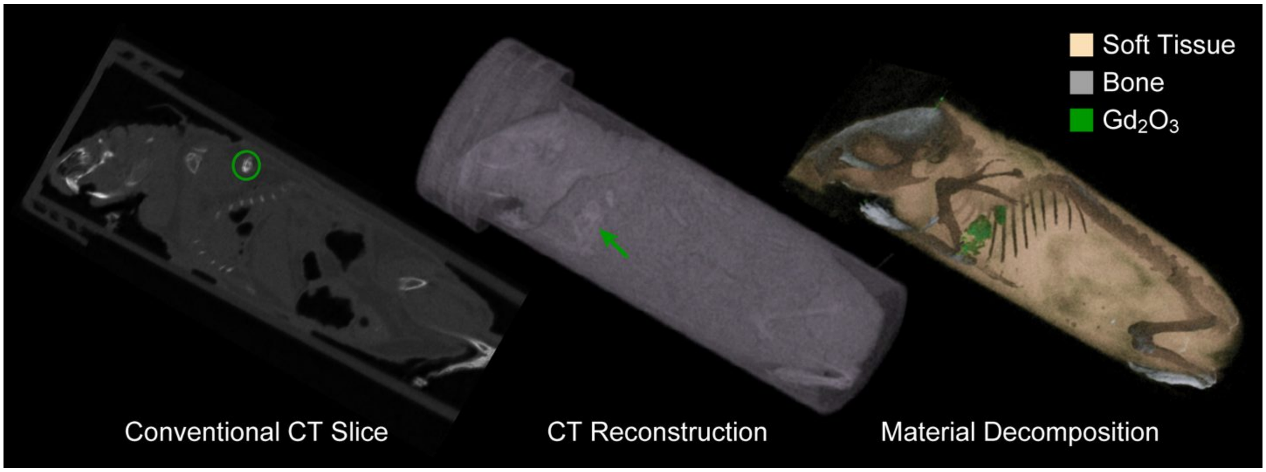

Figure 2. Conventional CT image slice, 3D reconstruction, and 3D material decomposition reconstruction acquired with a photon-counting spectral CT (MARS Bioimaging) showing a mouse after subcutaneous injection of 0.25 mL of 20 mM Gd_2O_3 (green labels) NPs post-mortem. Photon-counting spectral CT enabled the NP imaging probe to be clearly distinguished from skeletal tissue and other anatomic structures in the mouse.

3. DETECTION OF BREAST MICROCALCIFICATIONS

3.1. Significance

Microcalcifications (µcals) are the most common abnormality detected by mammographic screening for breast cancer, coincident with 30-50% of detected breast cancers [20]. However, the detection of µcals and correct diagnosis of breast cancer are limited by the sensitivity and specificity of mammography, especially in women with radiographically dense breast tissue which can mask abnormalities [21,22]. Therefore, bisphosphonate-functionalized gold NPs (BP-Au NPs) were developed as a targeted X-ray contrast agent for µcals due to the high binding affinity of BP for the hydroxyapatite (HA) mineral in µcals [7] and were shown to enable contrast-enhanced detection of breast µcals in both normal [23] and radiographically dense [24] mammary tissue *in vivo*.

3.2. Materials and Methods

Breast µcals were detected *in vivo* by targeted delivery of BP-Au NPs and contrast-enhanced CT. Au NPs, ~13 nm in diameter, were synthesized using the citrate reduction method and surface functionalized with alendronate, which provided a primary amine for binding to the Au NP surface opposite BP ligands for targeting calcium in HA µcals. The size distribution, colloidal stability, and HA binding affinity of BP-Au NPs was characterized in detail in previous studies [7,16]. A murine model of µcals was developed to allow for precise, *a priori* control over the level of mineral deposits within mammary glands (MGs) [23,24]. All studies were approved by the Institutional Animal Care and Use Committee at the University of Notre Dame. Microcalcifications were created by injecting the left number 4 MG with 50 µL of Matrigel (BD Sciences), a hydrogel comprised of extracellular matrix proteins, containing 0.5 or 5.0 mg/mL HA. The right MG was injected with 50 µL of Matrigel alone as a contralateral control. BP-Au NPs were administered to anesthetized mice by intramammary delivery 24 h after creating µcals in MGs at a total dose of 2 mg Au per mouse from 100 µL of 50 mM BP-Au NP solutions injected into each MG. Anesthetized mice were imaged *in vivo* by CT (Bruker Albira) immediately prior to delivering BP-Au NPs (0 h), and longitudinally at 3, 6, 24 and 48 h after delivering BP-Au NPs. CT images were acquired at 45 kVp, 400 µA, 250 ms integration time and 125 µm resolution for 600 slices with a 0.5 mm aluminum filter.

Quantitative molecular imaging of model breast µcals targeted by BP-Au NPs was investigated using photon-counting spectral CT. BP-PEG-Au NPs were prepared as described above except that a polyethylene glycol (PEG) linker was added between the Au surface and BP to further improve biostability. HA crystals were labeled with 50 mg/L of BP-PEG-Au NPs *in vitro* and the amount of NP binding was verified using ICP-OES. Model µcals were created in 10-week-old female FVB mice by injecting 100 µL of Matrigel containing 10 mg/mL Au-labeled HA into the fat pad of the right number 4 MG. Matrigel alone was injected into the left MG as a contralateral control. MGs were excised from the mice, embedded in 3% agarose, and imaged *ex vivo* using a photon-counting spectral micro-CT (MARS Bioimaging Ltd., Christchurch, NZ) with a 120 kVp source at 18 µA, 720 projections, ~300 µm resolution, and a 2 mm Al filter. Spectral CT used a photon-counting detector comprising a CdZnTe semiconductor bonded to a Medipix3RX ASIC (CERN) which enabled simultaneous image acquisitions within multiple energy bins [17], which were set at 7.0-30.9, 30.9-50, 50-60, 60-73, and 73-120 keV. Conventional CT images were acquired as the average of all energy bins. Quantitative material decomposition was performed using a quadratic programming algorithm (Matlab v9.0) with a maximum *a posteriori* estimator [18]. The material decomposition algorithm was calibrated to known concentrations including: air, water, calcium chloride solutions at 350, 700, 1050, and 1400 mM, and gold chloride solutions at 25, 50, 75, and 100 mM. The fractional abundance of detected Ca and Au were then assigned to color channels and scaled to mM concentrations.

3.3. Results and Discussion

BP-Au NPs targeted µcals and provided enhanced contrast for *in vivo* detection with conventional CT (Fig. 3a). Improved sensitivity was demonstrated by contrast-enhanced detection of µcals that were otherwise below the CT detection limit [23,24]. Improved specificity was demonstrated by contrast-enhanced detection of µcals that were above the CT detection limit, but difficult to distinguish from other structures of the breast (Fig. 3a), such as dense breast tissue [24]. The measured biodistribution of Au 48 h after delivery confirmed efficient targeting of BP-Au NPs to µcals, gradual clearance from the injection site, and low levels of uptake in the liver, spleen, and kidneys [23,24]. These results suggest that targeted NP imaging probes, such as BP-Au NPs, have the potential to improve sensitivity and specificity for the detection of breast abnormalities using conventional CT and mammography imaging systems. While potentially advantageous for translation, conventional systems do not permit quantitative material decomposition. However, photon-counting spectral CT enabled decomposition of the Ca and Au signals, and thus quantitative molecular imaging of the Ca and Au concentration in model µcals targeted by BP-PEG-Au NPs, rather than only relative differences in grayscale contrast as in conventional CT (Fig. 3b). This result suggests that the ability to detect separate and coincident signal from both the Au NP imaging probe and Ca µcal could provide greater confidence in distinguishing true positives from false positives.

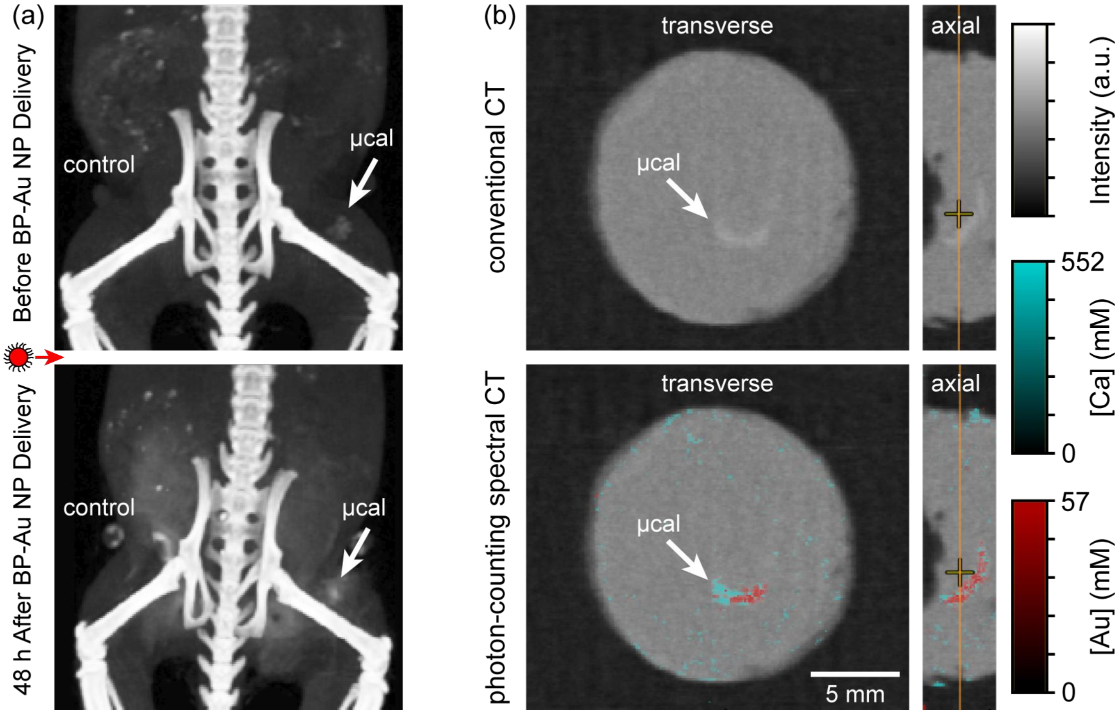

Figure 3. (a) Three-dimensional (3D) CT reconstructions showing microcalcifications (µcals) in murine mammary glands (arrows) before and 48 h after intra-mammary delivery of BP-Au NPs *in vivo*. BP-Au NPs enabled contrast-enhanced detection of µcals due to specific binding interactions, retention by µcals, and clearance from nontargeted tissue (contralateral control site). (b) Conventional and photon-counting spectral CT (MARS Bioimaging) images of an excised murine mammary gland containing a model µcal labeled by BP-PEG-Au NPs.

4. IMMUNOTARGETED IMAGING PROBES

4.1. Significance

Immunotargeting has emerged as a clinically successful therapeutic strategy for specific breast cancer subtypes, e.g., HER2+ breast cancer, which has led to research on immunotargeted imaging probes. The ability to target specific cancer subtypes and cell populations could enable improved diagnostic imaging for the early detection of recurrence or metastases, identification of the tumor margin in preoperative staging, and monitoring therapeutic progression [1-3]. Molecular imaging of cancer using various optical probes has become a powerful tool in preclinical research [25,26], but is only translatable to clinical diagnostic imaging of surface lesions due to the limited depth of penetration of visible and near-infrared light [27]. MRI, PET, and SPECT offer clinical molecular imaging and high sensitivity, but are often limited by low specificity, high cost, and/or the use of radiopharmaceuticals [12-15]. Combined anatomic and molecular imaging with CT would be advantageous due to the relatively high spatial resolution, low cost, and wide availability of CT, but must overcome the relatively low sensitivity of CT. The sensitivity of contrast-enhanced CT for detecting a small number of cells in a heterogeneous environment is not yet known.

Women diagnosed with ovarian cancer suffer high mortality and poor prognosis largely due to late diagnosis [29]. Improved detection of primary tumors and recurrence after chemotherapy is therefore crucial to reduce ovarian cancer mortality and improve progression free survival [27,29]. Ovarian cancer stem cells (CSCs) are thought to be a source of chemoresistant tumor metastases and biomarkers like CD133 are overexpressed in chemoresistant cells [30,31]. Therefore, immunotargeted NP imaging probes were investigated for targeting and identifying ovarian CSCs overexpressing CD133 using multimodal imaging. Core-shell NP imaging probes were designed to enable molecular imaging using both fluorescence for preclinical validation and CT for possible clinical translation.

4.2. Materials and Methods

Au@SiO$_2$ core-shell NPs were synthesized, volume-loaded with fluorophores, and immunoconjugated (Fig. 4a,b) using methods described in detail elsewhere [8]. The SiO$_2$ shell was volume-loaded with rhodamine B isothiocyanate (RITC) or DyLight 650, to provide red fluorescence, and bioconjugated with either IgG or anti-CD133, which was verified by protein agglomeration assay. SKOV3IP (ATCC) ovarian cancer cells were maintained in RPMI medium supplemented with 10% (v/v) fetal calf serum and 2 mmol/L L-glutamine in a 5% CO$_2$, 37°C incubator with 100% humidity. NPs were incubated for up to 24 h with SKOV3IP cells overexpressing either a CD133-GFP (green fluorescence protein) fusion protein or GFP-only as a negative control. Cells were imaged by epifluorescence microscopy and confocal microscopy. The binding kinetics and affinity was quantified by the fluorescence signal using both microscopy and flow cytometry.

Model tumors (Fig. 4e) were created by collecting and pelleting cells after incubation with NPs. SKOV3IP-CD133-GFP cells were trypsinized and fixed using 4% buffered para-formaldehyde. Fixed cells were transferred to 10 mM phosphate buffered saline, incubated with Au@SiO$_2$(RITC)-anti-CD133 NPs for 12 h at 4°C, and collected by centrifugation at 300 rcf for 5 min. The binding efficiency of the NP imaging probe was ~50%, which translated to 0.024 mg Au/10^6 cells. Control and immunotargeted cell pellets, ~2 mm in diameter, were embedded in phantoms comprising 2% agarose buffered with 10 mM PBS in 1.5 mL Eppendorf tubes using a biopsy punch to create a well that was backfilled with more agarose. Cell pellets were comprised of $2 \cdot 10^6$ cells in 12.5 µL which was pipetted into the agarose well. Phantoms were imaged by multispectral fluorescence (Bruker Xtreme) using a 12 cm field of view, F-stop of 1.1, and 0 mm focal plane. A Cy5 filter (excitation = 600-630 nm, emission = long pass 700 nm filter) was used for imaging DyLight 650 in NPs and a FITC filter (excitation = 475-495 nm, emission = long pass 530 nm filter) was used for imaging GFP in cells. Phantoms were also imaged by micro-CT (Scanco µCT-80) at 45 kVp, 177 µA, and 800 ms integration time for 720 projections, with a 10 µm voxel size and no beam filtration.

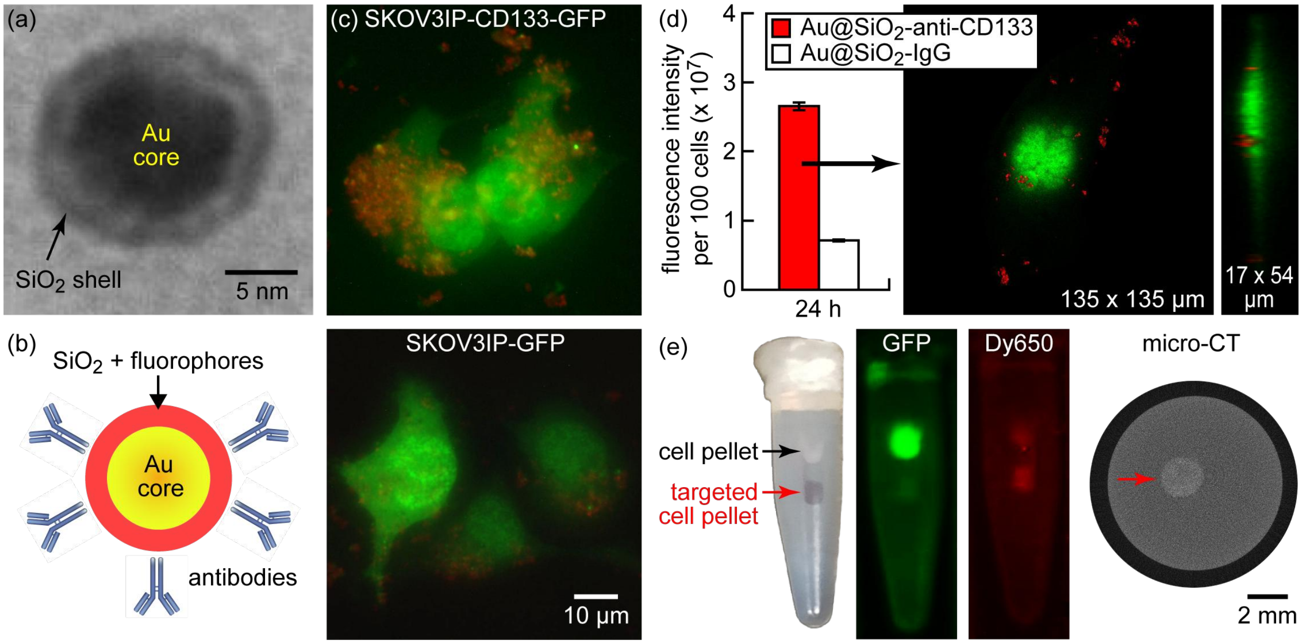

Figure 4. (a) Transmission electron micrograph of as-prepared Au@SiO$_2$ core-shell NPs and (b) schematic diagram showing Au@SiO$_2$(RITC)-anti-CD133 NPs designed for bimodal fluorescence and radiographic imaging, and immunotargeting ovarian cancer cells which overexpress CD133. Au@SiO$_2$(RITC)-anti-CD133 NPs exhibited specific targeting for CD133+ cells (SKOV3IP-CD133-GFP) compared with (c) control cells and (d) Au@SiO$_2$(RITC)-anti-IgG NPs after 4-24 h incubation *in vitro*. Both CD133+ and control cells also overexpressed GFP for visualization. (d) Cell surface targeting was confirmed with *z*-stack images in confocal microscopy. (e) Imaging phantom of model tumors comprising cell pellets embedded in agarose showing quenched but visible GFP signal and strong red fluorescence, and contrast-enhanced detection by micro-CT, of CD133+ cell pellets immunotargeted by Au@SiO$_2$(Dy650)-anti-CD133 NPs.

4.3. Results and Discussion

A modular platform was developed for preparing Au@SiO_2 core-shell NP imaging probes (Fig. 4a) designed for immunotargeting and multimodal imaging (Fig. 4b) [8]. Au@SiO_2(RITC)-anti-CD133 NPs exhibited target specific binding to overexpressed surface receptors on CD133+ cells and only limited non-specific binding to the extracellular matrix surrounding negative control cells or by isotype control NPs (Fig. 4c,d). After immunotargeting by Au@SiO_2(Dy650)-anti-CD133 NPs, CD133+ cell pellets exhibited quenched but visible GFP and strong red fluorescence. Importantly, Au@SiO_2(Dy650)-anti-CD133 NPs enabled contrast-enhanced detection of CD133+ cell pellets in micro-CT (Fig. 4e). Note that the concentration of Au within the cell pellet volume was ~20 mM, which was shown above to be detectable in a mouse (Fig. 2). Therefore, these results suggest that immunotargeted NP imaging probes and molecular imaging with CT may act synergistically to improve (1) early detection of small tumors and micrometastases, which will allow early treatment and thus improved progression free survival, and (2) quantitative assessment of therapeutic response for personalized treatment strategies. A comparable approach to non-invasively identify specific cell populations using an anatomic diagnostic imaging modality does not presently exist. Moreover, this approach may be effective at detecting small tumors and micrometastases which are currently not able to be detected in ovarian cancer patients resulting in delayed diagnosis and contributing to chemoresistance. Thus, this innovative approach could have a transformative impact on the diagnosis and treatment of recurrent ovarian cancer.

4. CONCLUSIONS

NP contrast agents and photon-counting detectors have synergistically transformed CT into a quantitative molecular imaging modality capable of multi-agent/material imaging in preclinical studies. In the future, immunotargeted NP imaging probes and molecular imaging with CT may also act synergistically to realize precision imaging for cancer detection and treatment.

ACKNOWLEDGMENTS

This research was supported by grants from the National Science Foundation (DMR-1309587), Kelly Cares Foundation, St. Joseph Regional Medical Center, Walther Cancer Foundation, and the University of Notre Dame Equipment Renewal and Restoration Program. The authors further acknowledge MARS Bioimaging (Christchurch, NZ), the Notre Dame Integrated Imaging Facility (NDIIF), the Notre Dame Center for Nanoscience and Nanotechnology (ND*nano*), and the Notre Dame Center for Environmental Science and Technology (CEST).

REFERENCES

[1] Herold, C. J., Lewin, J. S., Wibmer, A. G., Thrall, J. H., Krestin, G. P., Dixon, A. K., Shoenberg, S. O., Geckle, R. J., Muellner, A., Hricak, H., "Imaging in the Age of Precision Medicine," Radiology **279**(1), 226-238 (2016).

[2] Mankoff, D. A., Farwell, M. D., Clark, A. S., Pryma, D. A., "How Imaging Can Impact Clinical Trial Design: Molecular Imaging as a Biomarker for Targeted Cancer Therapy," Cancer J. **21**(3), 218-224 (2015).

[3] Collins, F. S., Varmus, H., "A New Initiative on Precision Medicine," N. Engl. J. Med. **372**, 793-795 (2015).

[4] Anderson, N. G., Butler, A. P., "Clinical applications of spectral molecular imaging: potential and challenges," Contrast Media Mol. Imaging **9**, 3-13 (2014).

[5] Jakhmola, A., Anton, N., Vandamme, T. F. "Inorganic Nanoparticles Based Contrast Agents for X-ray Computed Tomography," Adv. Healthcare Mater. **1**, 413-431 (2012).

[6] Cole, L. E., Ross, R. D., Tilley, J., Vargo-Gogola, T., Roeder, R. K., "Gold nanoparticles as contrast agents in X-ray imaging and computed tomography," Nanomedicine **10**(2), 321-341 (2015).

[7] Cole, L. E., Vargo-Gogola, T., Roeder, R. K., "Bisphosphonate-functionalized gold nanoparticles for contrast-enhanced X-ray detection of breast microcalcifications," Biomaterials **35**, 2312-2321 (2014).

[8] Nallathamby, P. D., Hopf, J., Irimata, L. E., McGinnity, T. L., Roeder, R.K., "Preparation of fluorescent Au-SiO_2 core-shell nanoparticles and nanorods with tunable silica shell thickness and surface modification for immunotargeting," J. Mater. Chem. B **4**, 17050-17062 (2016).

[9] McGinnity, T. L., Dominguez, O., Curtis, T. E., Nallathamby, P. D., Hoffman, A. J., Roeder, R. K., "Hafnia (HfO_2) nanoparticles as an X-ray contrast agent and mid-infrared biosensor," Nanoscale **8**, 13627-13637 (2016).

[10] Alessio, A. M., MacDonald, L. R., "Quantitative material characterization from multi-energy photon counting CT," Med. Phys. **40**, 031108 (2013).

[11] Kalender, W. A., "X-ray computed tomography," Phys. Med. Biol. **51**(13), 29-43 (2006).

[12] Elliott, A., "Medical imaging," Nucl. Instrum. Meth. A **546**, 1-13 (2005).

[13] Kircher, M. F., Willmann, J. K., "Molecular body imaging: MR imaging, CT, and US. Part I. Principles," Radiology **263**(3), 633-643 (2012).

[14] James, M. L., Gambhir, S. S., "A Molecular Imaging Primer: Modalities, Imaging Agents, and Applications," Physiol. Rev. **92**, 897-965 (2012).

[15] O'Connor, M. K., "Molecular breast imaging: an emerging modality for breast cancer screening," Breast Cancer Manag. **4**, 33-40 (2015).

[16] Ross, R. D., Cole, L. E., Tilley, J., Roeder, R. K., "Effect of Functionalized Gold Nanoparticle Size on X-Ray Attenuation and Binding Affinity to Hydroxyapatite," Chem. Mater. **26**(2), 1187-1194 (2014).

[17] Walsh, M. F., Nik, S. J., Procz, S., Pichotka, M., Bell, S. T., Bateman, C. J., Doesburg, R. M. N., De Ruiter, N., Chernoglazov, A. I., Panta, R. K., Butler, A. P. H., Butler, P. H., "Spectral CT data acquisition with Medipix3.1," J. Instrum. **8**, P10012 (2013).

[18] Curtis, T. E., Roeder, R. K., "Calibration methods influence quantitative material decomposition in photon-counting spectral CT," Proc. SPIE, 10132, 132 (2017).

[19] Deuerling, J. M., Rudy, D. J., Niebur, G. L., Roeder, R. K., "Improved accuracy of cortical bone mineralization measured by polychromatic micro-computed tomography using a novel high mineral density composite calibration phantom," Med. Phys. **37**(9), 5138-5145 (2010).

[20] Morgan, M. P., Cooke, M. M., McCarthy, G. M., "Microcalcifications Associated with Breast Cancer: An Epiphenomenon or Biologically Significant Feature of Selected Tumors?," J. Mammary Gland Biol. Neoplasia **10**, 181-187 (2005).

[21] Cheng, H. D., Cai, X., Chen, X., Hu, L., Lou, X., "Computer-Aided Detection and Classification of Microcalcifications in Mammograms: A Survey," Pattern Recogn. **36**, 2967-2991 (2003).

[22] Boyd, N. F., Martin, L. J., Yaffe, M. J., Minkin, S., "Mammographic Density and Breast Cancer Risk: Current Understanding and Future Prospects." Breast Cancer Res. **13**, 1-12 (2011).

[23] Cole, L. E., Vargo-Gogola, T., Roeder, R. K., "Contrast-enhanced X-ray detection of breast microcalcifications in a murine model using targeted gold nanoparticles," ACS Nano **8**(7), 7486-7496 (2014).

[24] Cole, L. E., Vargo-Gogola, T., Roeder, R. K., "Contrast-Enhanced X-ray Detection of Microcalcifications in Radiographically Dense Mammary Tissue Using Targeted Gold Nanoparticles," ACS Nano **9**(9), 8923-8932 (2015).

[25] Weissleder, R., Pittet, M. J., "Imaging in the era of molecular oncology," Nature 452, 580-589 (2008).

[26] Alford, R., Ogawa, M., Choyke, P. L., Kobayashi, H., "Molecular probes for the *in vivo* imaging of cancer. Mol. Biosyst. 5, 1279-1291 (2009).

[27] Kim, P. S., Djazayeri, S., Zeineldin, R., "Novel nanotechnology approaches to diagnosis and therapy of ovarian cancer," Gynecol. Oncol. **120**, 393-403 (2011).

[28] Cancer Facts and Figures 2013, American Cancer Society, Atlanta, GA (2013).

[29] Chung, H. H., Kang, W. J., Kim, J. W., Park, N. H., Song, Y. S., Chung, J. K., Kang, S. B., Lee, H. P., "Role of [18F]FDG PET/CT in the assessment of suspected recurrent ovarian cancer: correlation with clinical or histological findings," Eur. J. Nucl. Med. Mol. Imaging **34**(4), 480-486 (2007).

[30] Burgos-Ojeda, D., Rueda, B. R., Buckanovich, R. J., "Ovarian cancer stem cell markers: prognostic and therapeutic implications," Cancer Lett. **322**, 1-7 (2012).

[31] Steg, A. D., Bevis, K. S., Katre, A. A., Ziebarth, A., Dobbin, Z. C., Alvarez, R. D., Zhang, K., Conner, M., Landen, C. N. "Stem cell pathways contribute to clinical chemoresistance in ovarian cancer," Clin. Cancer Res. **18**, 869-881 (2012).